Zhang, N., Pasciak, M., Glazer, A. M., Hlinka, J., Gutmann, M., Sparkes, H. A., Welberry, T. R., Majchrowski, A., Roleder, K., Xie, Y., & Ye, Z. G. (2015). A neutron diffuse scattering study of $PbZrO_3$ and Zr-rich $PbZr_{1-x}Ti_xO_3$. *Journal of Applied Crystallography*, *48*(6), 1637-1644. https://doi.org/10.1107/S1600576715017069

JOURNAL OF APPLIED CRYSTALLOGRAPHY
ISSN 1600-5767

A neutron diffuse scattering study of $PbZrO_3$ and Zr-rich $PbZr_{1-x}Ti_xO_3$

Nan Zhang,[a,b] Marek Paściak,[c] A. M. Glazer,[d,e]* Jirka Hlinka,[c] Matthias Gutmann,[f] Hazel A. Sparkes,[f] T. R. Welberry,[g] Andrzej Majchrowski,[h] K. Roleder,[i] Yujuan Xie[b] and Zuo-Guang Ye[a,b]

[a]Electronic Materials Research Laboratory, Key Laboratory of the Ministry of Education and International Centre for Dielectric Research, Xi'an Jiaotong University, Xi'an, 710049, People's Republic of China, [b]Department of Chemistry and 4D LABS, Simon Fraser University, 8888 University Drive, Burnaby, BC, Canada, V5A 1S6, [c]Institute of Physics, The Academy of Sciences of the Czech Republic, Na Slovance 2, 182 21 Prague 8, Czech Republic, [d]Department of Physics, University of Oxford, Parks Road, Oxford OX1 3PU, UK, [e]Department of Physics, University of Warwick, Coventry CV4 7AL, UK, [f]ISIS Facility, Rutherford Appleton Laboratory, Chilton, Didcot OX11 0QX, UK, [g]Research School of Chemistry, Australian National University, Canberra, ACT 2601, Australia, [h]Institute of Applied Physics, Military University of Technology, ulica Kaliskiego 2, Warsaw 00-908, Poland, and [i]Institute of Physics, University of Silesia, ulica Uniwersytecka 4, Katowice 40-007, Poland. *Correspondence e-mail: michael.glazer@physics.ox.ac.uk

Received 18 June 2015
Accepted 11 September 2015

Edited by Th. Proffen, Oak Ridge National Laboratory, USA

Keywords: neutron diffraction; diffuse scattering; lead zirconate titanate; disorder; short-range order.

Supporting information: this article has supporting information at journals.iucr.org/j

A combined neutron diffuse scattering study and model analysis of the antiferroelectric crystal $PbZrO_3$ is described. Following on from earlier X-ray diffuse scattering studies, supporting evidence for disordering of oxygen octahedral tilts and Pb displacements is shown in the high-temperature cubic phase. Excess diffuse scattering intensity is found at the *M* and *R* points in the Brillouin zone. A shell-model molecular dynamics simulation closely reproduces the neutron diffuse scattering pattern. Both in-phase and antiphase tilts are found in the structural model, with in-phase tilts predominating. The transition between disordered and ordered structure is discussed and compared with that seen in Zr-rich $PbZr_{1-x}Ti_xO_3$.

1. Background

Antiferroelectric (AFE) materials are widely used in transducers, energy-storage devices and microelectromechanical systems. The very first identified antiferroelectric material was $PbZrO_3$ (PZ) (Kittel, 1951; Shirane *et al.*, 1951; Sawaguchi & Kittaka, 1952), an end member of the well known piezoelectric solid solution $PbZr_{1-x}Ti_xO_3$ (PZT). Both PZ and PZT belong to the perovskite family, having the cubic $Pm\bar{3}m$ aristotype structure above the Curie temperature. At room temperature, PZ displays a complex centrosymmetric structure (space group *Pbam*) (Glazer *et al.*, 1993; Corker *et al.*, 1997), involving antiparallel displacements of the cations on the (110) planes and oxygen octahedral tilts (type $a^-a^-c^0$ in the Glazer notation; Glazer, 1972). Between the room-temperature AFE phase and the high-temperature paraelectric (PE) phase, a dielectric anomaly was discovered many years ago, and this was suggested to be related to a ferroelectric (FE) intermediate phase (Scott & Burns, 1972; Dai *et al.*, 1995), whose presence still remains controversial (Fujishita & Hoshino, 1984; Teslic & Egami, 1998). Density functional theory calculations show that, with the oxygen octahedral tilts included, the AFE *Pbam* state and an FE *R*3*c* state are very close in energy (Reyes-Lillo & Rabe, 2013; Íñiguez *et al.*, 2014). The compositional phase boundary between the AFE and FE phases in the PZT phase diagram is around $x = 0.07$ (Woodward *et al.*, 2005). The neighbouring FE phase is

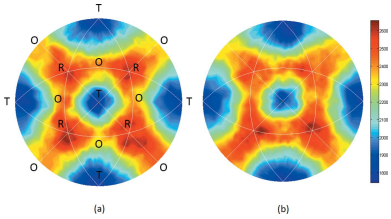

rhombohedral $R3c$ with $a^-a^-a^-$ tilts at low temperature and no tilts ($a^0a^0a^0$) at high temperature.

For PZ, the room-temperature tilt system $a^-a^-c^0$ corresponds to the condensation of distortion modes at the R point in the Brillouin zone [with Zr chosen to lie on the unit-cell origin this mode is labelled R_4^+ (*ISOTROPY Software Suite*; http://iso.byu.edu)] involving antiphase oxygen octahedral tilts on successive layers about the tilt axes along [100] and [010], respectively. However, electron diffraction experiments on PZT (x = 0.05) (Xu *et al.*, 1995; Viehland, 1995) have found evidence for M-type distortions (labelled M_3^+), which would imply tilts occurring in phase on successive layers. At high temperature, the cubic phase is considered to be the simplest structure in the perovskite family, with all the atoms at special positions fixed by the crystallographic symmetry. Nonetheless, recent studies have shown that for materials like PZ or PZT the structure above the Curie temperature T_c may be much more complex. Kuroiwa *et al.* (2005) carried out high-energy synchrotron radiation powder diffraction experiments for PZT in the cubic phase. They suggested that the Pb atoms were disordered[1] by being displaced from their high-symmetry positions. In addition, high-resolution neutron diffraction experiments further revealed disordering of oxygen octahedral tilts, as indicated by anisotropic displacement ellipsoids in the form of flat discs perpendicular to ⟨111⟩ in the Zr-rich region (Zhang *et al.*, 2011). A recent combined pair distribution function (PDF) analysis coupled with Rietveld refinement of neutron diffraction data (Zhang *et al.*, 2014) has confirmed that at room temperature, for the same Zr-rich compositions, there exists a local structure in PZT that is very different from the average structure. This was interpreted as a coexistence of long-range rhombohedral and short- and long-range monoclinic symmetries involving the different cation displacement directions of Pb. In pure PZ, in addition to local Pb displacements, oxygen octahedral tilting is another crucial component in determining the local structure above T_c.

Recently, there have been a few reports of X-ray diffuse scattering (DS) in PZ or PZT (Paściak *et al.*, 2015; Burkovsky *et al.*, 2014, 2012; Hlinka *et al.*, 2011). Tagantsev *et al.* (2013) observed anisotropic intensity distributions around certain Bragg peaks at 553 K, suggesting that the antiferroelectric phase of PZ is driven by a ferroelectric instability through a flexoelectric coupling. First-principles simulations reveal the primary role that the R_4^+ mode plays in the transition from the cubic phase to the AFE orthorhombic phase (Mani *et al.*, 2015). The condensation of the octahedral tilts in the antiferroelectric phase was inferred to be caused by trilinear (Hlinka *et al.*, 2014; Íñiguez *et al.*, 2014) and biquadratic (Tagantsev *et al.*, 2013) coupling terms. Paściak *et al.* (2015) carried out X-ray DS experiments in a wide range and presented shell-model molecular dynamics (MD) simulations that gave results in very good agreement with experimental observations. Different features of the X-ray DS patterns have been attributed to lead- or oxygen-dominated displacement modes; however, no in-depth local structure analysis has been presented. It is also worth mentioning that in PZ single crystals, above the structural phase transition at T_c, precursor polar clusters were suggested to be formed in the paraelectric phase, which grow rapidly upon cooling, starting at 50 K above T_c, *i.e.* at 553 K. This suggestion was based on observations of finite birefringence and the piezoelectric effect (Ko *et al.*, 2013).

However, there have never been any neutron diffuse scattering experiments on this material, which should reveal any disorder in the oxygen octahedra more prominently. In the present study, we have collected and analysed simultaneously high-quality Bragg diffraction and neutron diffuse scattering data for PZ at 523 K. Experimental DS patterns are compared with the ones calculated from shell-model structures obtained with MD simulation. To further complement the previous work on this model, the short-range order features for both cations and octahedral tilts are discussed in detail. We also compare the observed neutron diffuse scattering with that from a crystal of $PbZr_{0.69}Ti_{0.31}O_3$.

2. Methods

2.1. Single-crystal growth of $PbZrO_3$

Spontaneous crystallization of lead zirconate was carried out from a high-temperature solution containing 2.4 mol% of PbZrO3, 77 mol% of Pb ions (from Pb_3O_4) and 20.6 mol% of B_2O_3 (140 g in total). $PbZrO_3$ melts incongruently at 1843 K (Fushimi & Ikeda, 1967). To ensure crystallization below the temperature of the peritectic transition, an excess of PbO was used as a self-flux. Addition of B_2O_3 allows further lowering of the crystallization temperature range and therefore limited evaporation losses. We used Pb_3O_4 instead of PbO to improve the quality of the as-grown PZ single crystals; use of PbO solvent leads to growth of dark-grey PZ crystals, while Pb_3O_4 solvent guarantees crystallization of totally transparent colourless samples. The growth was carried out in a Pt crucible covered with a Pt lid and placed in a single-zone resistance furnace that was thermally isolated also from the top. The resulting axial temperature gradient was lower than 5 K cm^{-1}. The melt was soaked at 1420 K and then its temperature, measured at the bottom of the Pt crucible, was lowered at a rate of 2.5 K h^{-1} down to 1190 K. At that temperature the melt was decanted and the as-grown PZ crystals were cooled to room temperature at a rate of 10 K h^{-1}. To remove traces of the solidified melt the crystals were etched in dilute acetic acid.

2.2. Neutron single-crystal diffraction

A colourless PZ single crystal measuring 5 × 2 × 2.5 mm and a smaller $PbZr_{0.69}Ti_{0.31}O_3$ single crystal of around 1.5 × 2 × 3 mm were both measured at room temperature and at 523 K at ISIS (Rutherford Appleton Laboratory) on SXD (Keen *et al.*, 2006). Using the time-of-flight Laue technique, a large three-dimensional region of reciprocal space was

[1] Note: the term 'disorder' as used in this paper does not necessarily mean that it is of static origin, but it may indicate the presence of low-frequency local modes.

recorded by 11 detectors surrounding the sample chamber. By controlling the rotation angles for each exposure, complete mapping of reciprocal space was achieved. The average Q resolution with different time-of-flight and detector angles is around 1% $\Delta Q/Q$. The integration of the data and the sample holder as well as the background corrections were made using the software *SXD2001* (Gutmann, 2005). The diffraction patterns on (*hkl*) planes were then extracted after applying $m\bar{3}m$ Laue symmetry (Welberry *et al.*, 2005).

2.3. Shell model and molecular dynamics simulations

The shell model we use here has been already described in detail (Paściak *et al.*, 2015). This is a classical model of interactions where each atom is represented by a core and shell to mimic atomic polarization. There are short-range interactions between shells, Coulombic interactions between all the particles except for cores and shells of the same atom which are bounded by an anharmonic spring [see Sepliarsky *et al.* (2005) for examples of the use of the shell model for some other perovskite systems]. The parameters of the model were obtained by fitting first-principles results obtained for PZ.

MD simulations were performed in the cubic phase, at a temperature 25 K above the phase transition within a constant temperature/constant strain ensemble, using the software *DLPOLY* (Todorov *et al.*, 2006). The time step was set to Δt = 0.4 fs, and structures of the size 50 × 50 × 50 cubic unit cells were equilibrated for 4 × 10^5 time steps. In order not to exclude dynamical disorder we analysed instantaneous structures obtained within a production run (after equilibration). As in the previous contribution exploring the same model, we concentrate here on four such snapshot structures collected at different time instants with the time interval being 2 ps.

3. Results and discussion

Structure refinement of the PZ data at 523 K was first performed using the software *JANA2006* (Petricek *et al.*, 2014). The lattice constant was 4.1586 (3) Å, which is similar to the results from Rietveld refinement (Zhang *et al.*, 2011). The structural model used space group $Pm\bar{3}m$ with anisotropic displacement parameters (ADPs). In the case of Pb and Zr cations, the displacement parameters are fixed by symmetry to be isotropic. However, the ADPs for the oxygen atoms follow the symmetry restrictions $U^{11} = U^{22} \neq U^{33}$; $U^{12} = U^{13} = U^{23} = 0$. The values of the refined ADPs are listed in Table 1. For oxygen, the U^{11} value is more than ten times larger than U^{33}, making the oxygen ellipsoid extremely flat on the {001} planes (Fig. 1*a*). This agrees well with our previous powder neutron diffraction results on PZ and Zr-rich PZT (Zhang *et al.*, 2011), which suggested that disordered octahedral tilting was either a remnant of the long-range tilting seen at lower temperatures on heating or the precursor to the same on cooling. The analysis above is based on conventional refinements of the Bragg diffraction data, in which case the ADPs are all harmonic, while anharmonic displacements are usually considered to have a negligible influence on the Bragg intensities. However, anharmonicity should be taken into account in discussing the order–disorder phenomena when the ADPs are large. In such cases, the Gram–Charlier expansion is commonly used (Boysen, 1992; Kiat *et al.*, 2000). For the high-temperature cubic perovskite structure, because of the centrosymmetry of the sites, all the second-order anharmonic tensors are zero. We therefore carried out refinement in fourth order; three fourth-order components (D^{1111}, D^{2222} and D^{1122}) for the oxygen atoms are then obtained. This application of anharmonic ADPs leads to an octahedral-shape nuclear density centred on the oxygen positions (Fig. 1*b*). The vertices of the octahedral shape are extended along the ⟨100⟩ directions, which are the oxygen displacement directions for octa-

Table 1
Values of anisotropic displacement parameters obtained in the structure refinement of PZ at 553 K.

	U^{11} (Å^2)	U^{33} (Å^2)
Pb	0.0599 (4)	–
Zr	0.0076 (1)	–
O	0.0641 (4)	0.0051 (2)

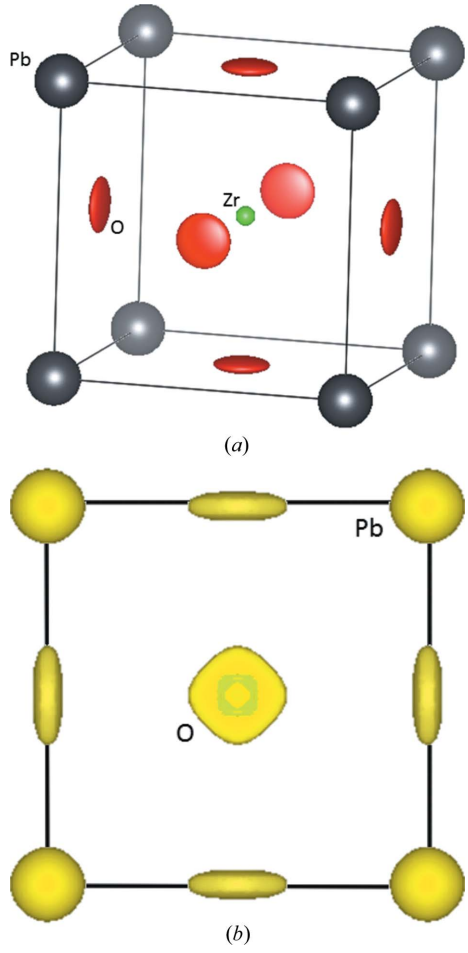

Figure 1
(*a*) Plot of the $PbZrO_3$ structure in the cubic phase with anisotropic ellipsoids for oxygen (red); (*b*) (001) projection of the nuclear density around the oxygen positions after refining anharmonic ADPs.

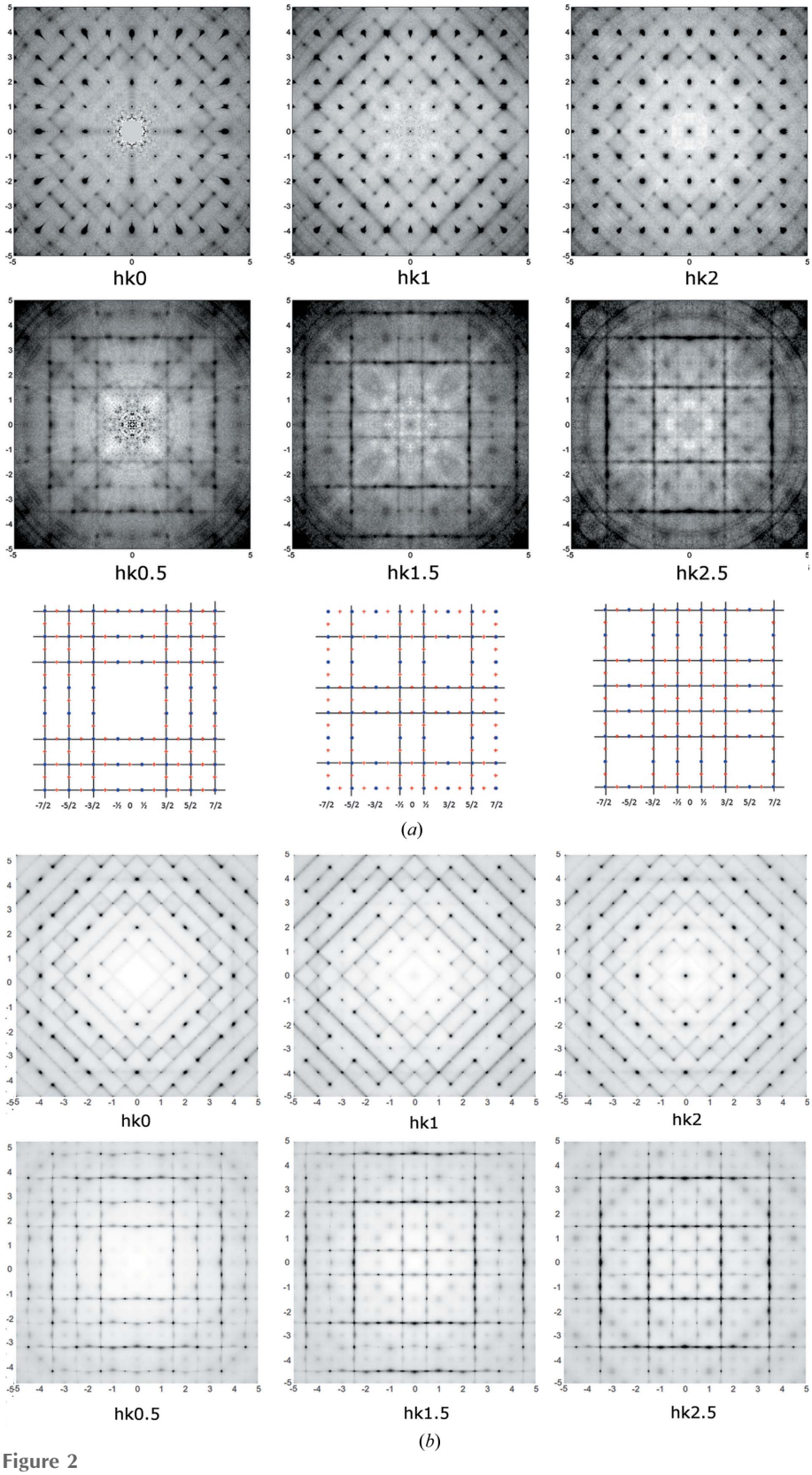

Figure 2
(*a*) Neutron diffuse scattering patterns of $PbZrO_3$ at 523 K for *hkn*, *n* integer and half-integer. The bottom three diagrams show the positions of the plus and minus tilt reflections on the half-layers using blue dots (*R* points, – tilts) and red crosses (*M* points, + tilts), and the directions of the observed streaks (black lines along *R*–*M*) in each case. (*b*) Simulated neutron diffuse scattering patterns calculated using the program *DISCUS* from structures obtained with shell-model MD simulation. The average structure's Bragg scattering has been subtracted from the total intensity.

hedral tilts. This further supports our model of disordered tilting in the cubic phase of PZ.

Plots of the neutron scattering patterns on the main Bragg layers (*hk*0, *hk*1 and *hk*2) and on the superlattice layers (*hk*0.5, *hk*1.5 and *hk*2.5) are shown in Fig. 2(*a*). On the main layers, in addition to the Bragg peaks with strong intensity, there is evidence of fainter scattering localized at the *M* points (related to plus tilts), *e.g.* $\frac{3}{2}\frac{5}{2}0$, $\frac{1}{2}\frac{3}{2}1$, $\frac{7}{2}\frac{5}{2}2$ *etc*. All the half-integer reflections with $h = k$ are absent, which agrees with the rules for observing the octahedral tilt peaks (Glazer, 1975). There are discontinuous streaks in the ⟨110⟩ directions on all the main layers, connecting two weak *M* point reflections. More interesting patterns are observed on the superlattice layers. Weak intensities are found at *h*/2 *k*/2 *l*/2 positions, and the intensity is absent when $h = k = l$. This type of absence is consistent with the rules for antiphase octahedral tilting (Glazer, 1975). In fact, if all the possible plus and minus octahedral tilt reflections are plotted (bottom three drawings in Fig. 2*a*), it is seen that they fit perfectly with the observed intensities on the middle three images. In addition to the scattering at *R* and *M* points, there are streaks along the [100] and [010] directions passing through these points, which are absent when passing through points with two odd indices the same, thus avoiding the forbidden indices $h = k = l$. All these observations indicate strongly that there is a certain level of disordering along the streak directions, which is closely related to the oxygen octahedral tilts.

To get more insight into the local structure and octahedron tilt disorder we turn to analysis of shell-model structural configurations obtained with molecular dynamics simulation. It was shown previously (Paściak *et al.*, 2015) that the model can reproduce X-ray diffuse scattering features including these assigned to tilting. Moreover, the refined octahedral-shape nuclear density distribution at the oxygen positions (Fig. 1*b*) from the neutron diffraction data is very similar to the results of MD simulation, as shown in

Fig. 3 of Paściak *et al.* (2015). To further validate the suitability of the model, neutron DS patterns were calculated (using the program *DISCUS*; Proffen & Neder, 1997). As is clear from Fig. 2(*b*), most of the features discussed above are reproduced in the calculated patterns. On the *hk*0 layer, the ⟨110⟩ streaks corresponding to cation short-range order are shown, and an abrupt intensity change is present at the *M* points. On the *hk*0.5, *hk*1.5 and *hk*2.5 layers, the *M* and *R* points are all clearly shown. The [100] and [010] streaks on these two layers are at the same positions as in the observed pattern, and even the slight bending of the streaks around the *M* points is successfully reproduced.

With such a good agreement between the calculated and observed patterns, we investigated the details of the short-range order predicted by the model. Fig. 3 shows a plot of a layer of the structure extracted from the calculation where most of the octahedra are seen to maintain a rigid-body structure while rotating in clockwise or anticlockwise directions about the *z* axis. In the analysis of tilts we concentrate on (001) planes (*z* layers): the structures, however, have average cubic symmetry and the same features are found on symmetry-related *x* and *y* layers. The tilts generally exist in many areas on different *z* layers (we scanned every layer through the whole volume of each structure).

Fig. 4(*a*) shows a schematic drawing for a typical layer perpendicular to *z*. In the drawing, each small cell represents one unit cell on the *xy* plane. The colours represent the tilt directions of the octahedra about the *z* axis: if the octahedron rotates anticlockwise, the cell it belongs to is coloured blue; if it rotates clockwise, the cell is coloured red; if the octahedron shows no obvious rotation, the cell is left blank. Therefore, if blue and red cells appear consecutively over several cells, they form a correlated tilted region. The figure shows that a complete tilted region on any one layer is relatively small, but they appear very frequently. To identify the tilting types, one needs to compare the tilt arrangements on three contiguous

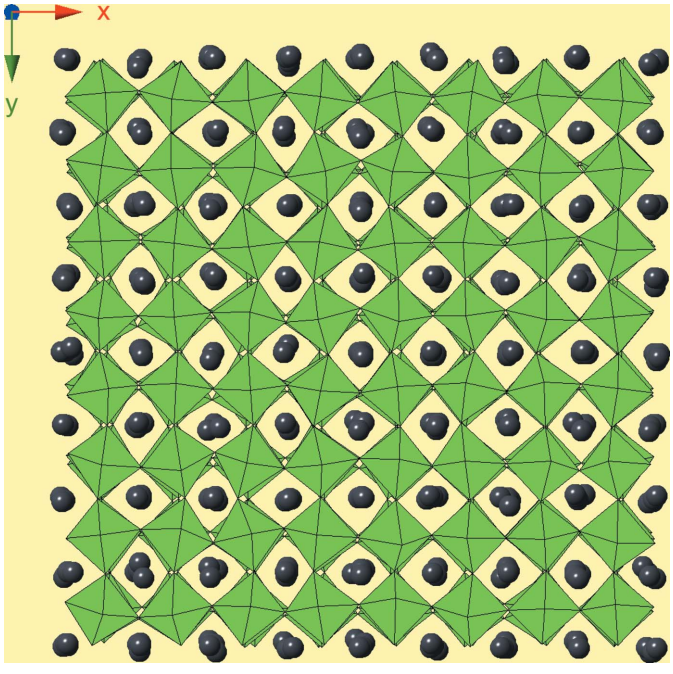

Figure 3
Plot of a typical layer in the PZ structure on a (001) plane extracted from the MD simulation.

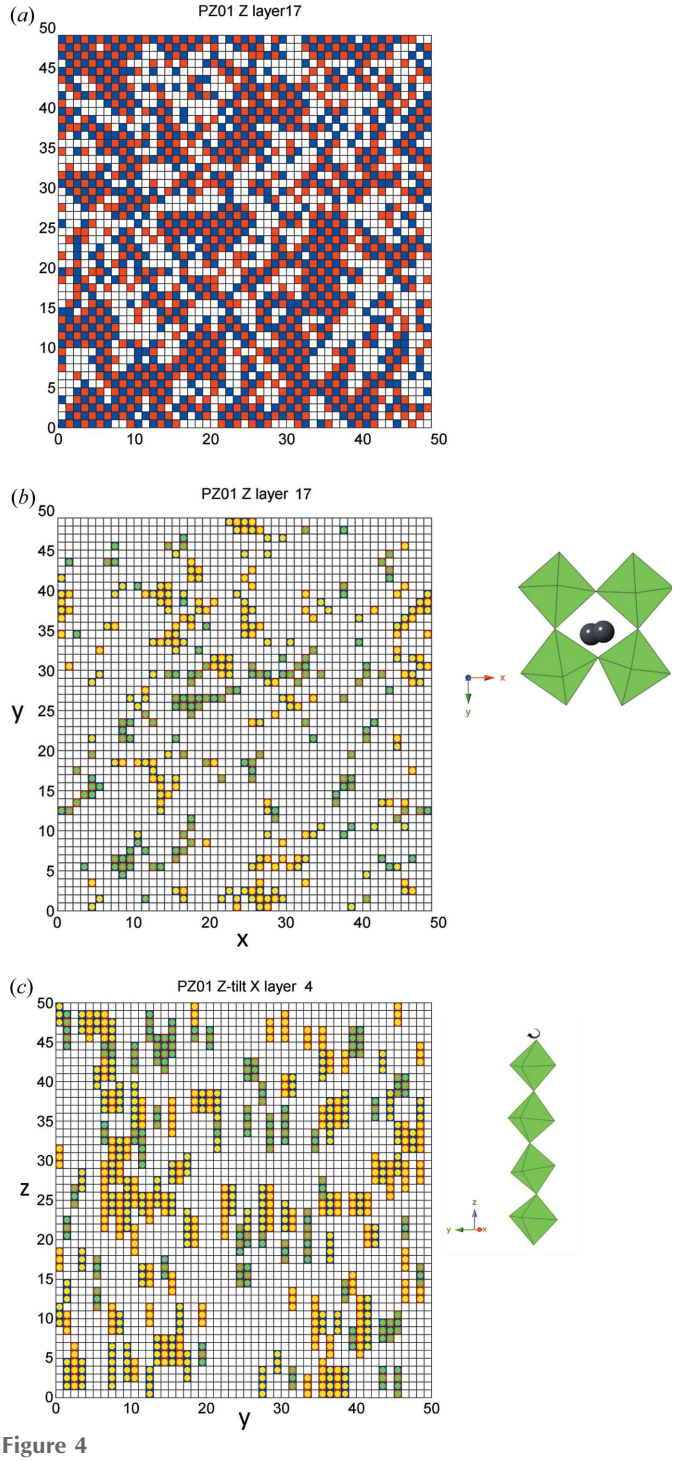

Figure 4
(*a*) Unit-cell rotation arrangements on the 17th *z* layer from one MD simulation model: blue stands for anticlockwise rotations and red for clockwise rotations (around the *z* axis). (*b*), (*c*) Tilt types around the *z* axis are obtained by comparing the rotations on three neighbouring *z* layers. Yellow areas correspond to in-phase (c^+) tilts and green areas to antiphase (c^-) tilts. (*b*) is viewed along *z* on the 17th *z* layer, and (*c*) is viewed along *x* on the 4th *x* layer. Note that equivalent diagrams for *x*- and *y*-type tilts show similar correlations.

neighbouring z layers: if the same regions have the same blue–red pattern, this indicates an in-phase tilt c^+ (M_3^+ mode); if they have opposite palette patterns between each layer, this indicates an antiphase tilt c^- (R_4^+ mode). We coloured the unit cells on each layer by comparing with the previous and the next layer: yellow for in-phase tilts and green for antiphase tilts. Fig. 4(*b*) is a typical example as a result of the comparison between three consecutive layers. We can see from the figure that the in-phase tilted areas (yellow) are generally larger than antiphase tilted areas (green). Fig. 4(*c*) demonstrates the correlations along the z axis by viewing the structure on a yz plane. The yellow columns contain cells with the same directions of rotations along z, indicating in-phase tilts; the columns with antiphase tilts, containing cells with opposing rotation directions along z, are green. More and longer in-phase correlations are found in Fig. 4(*c*) than antiphase correlations.

Quantitative analyses also support this observation by taking account of the statistics from all 50 independent layers of the simulation box at four different time instances. Fig. 5(*a*) shows the appearing frequencies of c^+ and c^- regions as a function of area, while Fig. 5(*b*) shows the frequencies against length. It is clear that the plus-tilted regions have a larger range of areas (1–80 unit cells) and lengths (3–13 unit cells) compared with the minus-tilted regions (1–28 unit cells for areas and 3–9 unit cells for lengths). Although very small tilted areas and lengths occur for more than 50% of cases, their frequencies drop more dramatically with larger areas or lengths for minus tilts, indicating that there are fewer minus-tilted regions with lengths spanning beyond three or four unit cells than plus-tilted regions. Note that, although the low-temperature *Pbam* phase has only out-of-phase tilts ($a^-a^-c^0$), and the possible intermediate phase (Tan *et al.*, 2011) or the neighbouring *R*3*c* phase in the PZT phase diagram involves only out-of-phase tilts as well, there is a considerably larger number of in-phase tilts above the Curie temperature. This implies that cubic precursor fluctuations, having a majority of in-phase correlations, are not directly associated with the frozen minus tilts that are triggered as a secondary order parameter in the AFE transition. The tilt angle values, on the other hand, are about the same for the regions with in-phase and out-of-phase tilt correlations with respect to the adjacent layer. Fig. 5(*c*) is a histogram of the tilt angles, with in-phase tilts marked positive and out-of-phase tilts marked negative. Apart from the fact that there are more positive tilts than negative, the peak positions for these two types are similar, both around 6°. The average absolute value of the tilt angles marked as positive is 6.0 ± 2.5°, and the average absolute value of the tilt angle marked as negative is 5.6 ± 2.4°.

In our neutron diffuse scattering pattern for $PbZr_{0.69}Ti_{0.31}O_3$ single crystals at various temperatures, we observed similar phenomena (Fig. 6*a*). For PZT single crystals at this composition, the average structure starts from the tilted *R*3*c* phase at room temperature, changes into the untilted *R*3*m* phase at around 373 K and becomes cubic at 610 K (Xie, 2013). In the room-temperature diffraction pattern, on the superlattice layers, in addition to the *R* points for *R*3*c*, there are also weak intensities at *M* points. This indicates that for

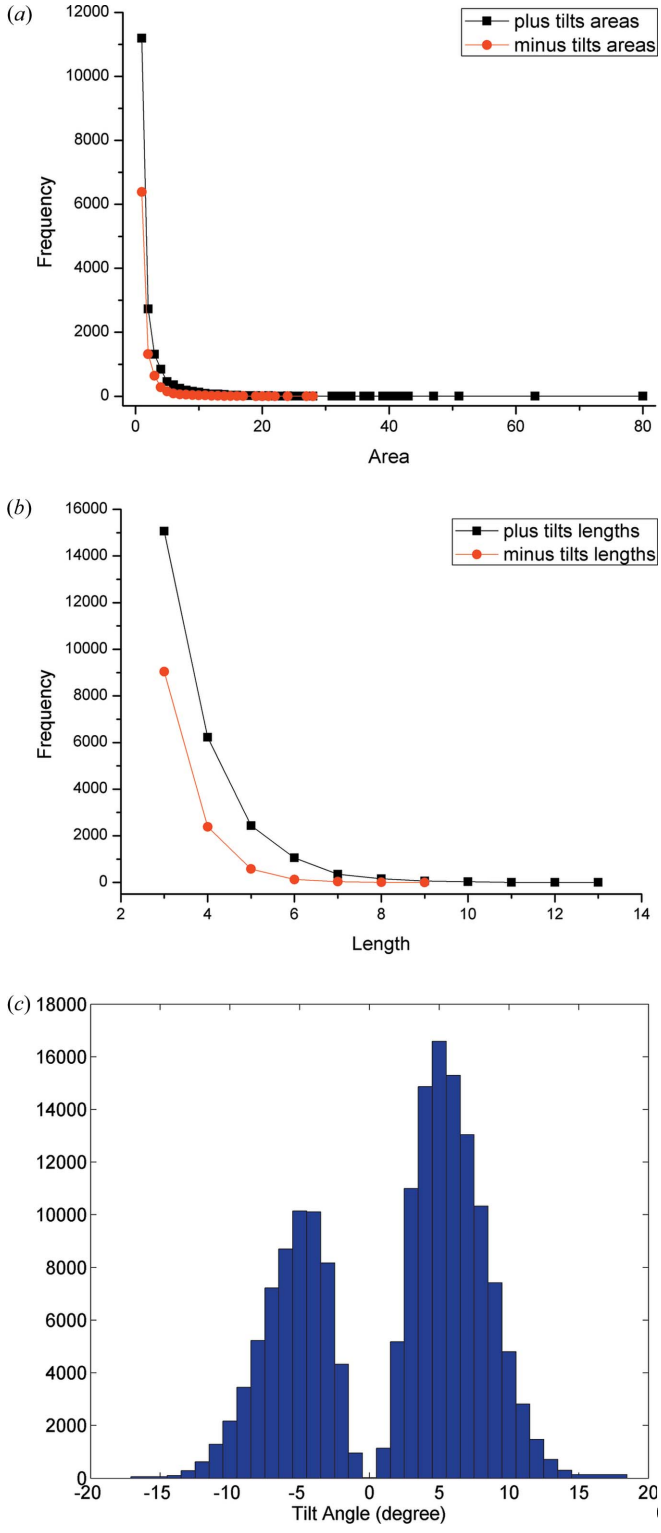

Figure 5
(*a*) Frequency of c^+ and c^- regions as a function of area. The areas stand for the number of unit cells of a continuous region in the form of either in-phase or antiphase tilts on a single z plane. (*b*) Frequency against length in the z direction continuously for either tilt type. The areas for plus tilts range from one to 80 unit cells and those for minus tilts from one to 28. The lengths range from three to 13 unit cells for plus tilts and three to nine unit cells for minus tilts. Similar results can be obtained for tilts about the other axes. (*c*) Histogram of tilt angle distribution. The plus tilt angles are positive values and minus tilt angles are negative values.

unit cells viewed down the x, y or z axes there are some in-phase tilt components interrupting the generally large anti-phase tilted regions, generating a stacking-fault-like effect, as illustrated in Fig. 6(b). At 523 K, the $R3c$ phase changes into $R3m$ by losing the minus tilts on average. However, in the diffuse scattering pattern we still observed streaks passing through the half indices, similar to the diffuse scattering patterns of PZ, with higher intensities around the M points. This also shows that, when the low-temperature ordered antiphase tilts become disordered in the $R3m$ phase, the in-phase tilts remain together with antiphase tilts, possibly discontinuously, in smaller local regions. With this trend, it is expected that above the Curie temperature the disordered local tilts should still persist as in PZ. This is in good agreement with the flat-shaped oxygen anisotropic displacement ellipsoids in the cubic phase observed not only in PZ but in many Zr-rich PZT compositions (Zhang *et al.*, 2011).

We also calculated the local Pb displacements from the MD-derived structures for PZ in the cubic phase. The average absolute value of the magnitude of displacement is 0.3 ± 0.1 Å, which is equivalent to a fractional coordinate pseudocubic cell value of 0.08, within the range of the average displacement lengths seen for the orthorhombic *Pbam* phase. The distributions of the displacement directions are plotted on a stereographic projection viewed down the [001] direction in Fig. 7. The technical details for this type of plot can be found in the papers by Zhang *et al.* (2014) and Keeble *et al.* (2013). Instead of being randomly displaced in all directions, the displacement distributions are clearly clustered around the eight rhombohedral directions (marked R) and on the monoclinic mirror planes, similar to what has been observed for Pb-based ferroelectric relaxors (Paściak *et al.*, 2012). Most of the local monoclinic displacements correspond to monoclinic M_B (Vanderbilt & Cohen, 2001) structures, as they lie on the mirror planes with the displacements between rhombohedral (triad) and orthorhombic (diad) directions. In our previous PDF study (Zhang *et al.*, 2014) on Zr-rich PZT at room temperature, this type of short-range monoclinic disor-

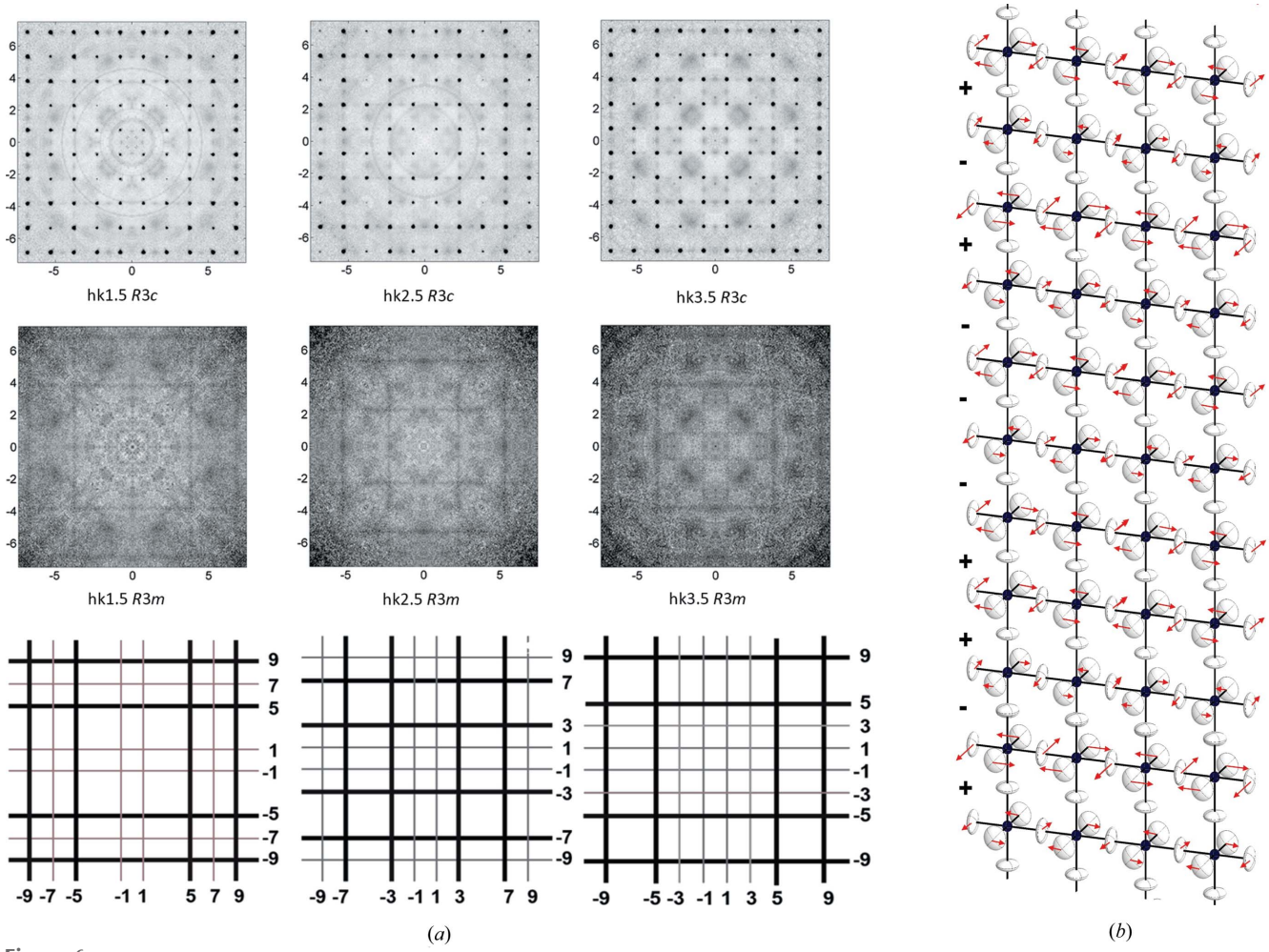

Figure 6
(a) Neutron diffuse scattering patterns for a $PbZr_{0.69}Ti_{0.31}O_3$ crystal on different superlattice layers at room temperature (the first row) and at 523 K (the second row). The bottom three diagrams show the directions of the observed streaks (thick black lines) in each case. Numbers in the figures are for double pseudocubic unit cells, so all the half-layer numbers are shown as odd numbers in this case. (b) Schematic diagram showing octahedral tilt components based on the DS pattern in (a), where alternating plus and minus tilting about the c axis is marked by red arrows, with related octahedra along the b axis. Octahedra along the a-axis direction are not shown in order to avoid clutter.

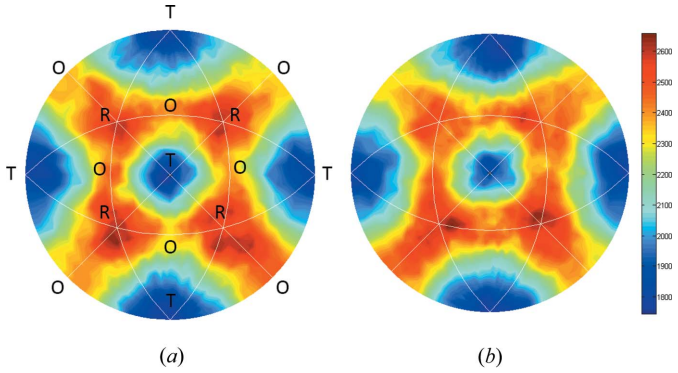

(*a*) (*b*)

Figure 7
Stereographic projections for Pb atomic displacements from the shell-model calculation. (*a*) shows observations on the front stereographic hemisphere, while (*b*) is for the hemisphere behind. The viewing direction is down [001]. The tetragonal (T), rhombohedral (R) and orthorhombic (O) cation displacement directions for perovskites are marked on the front figure. The white lines are the mirror planes corresponding to displacements with monoclinic symmetry. The colour scale is in arbitrary units.

dering was discovered and, near the PZ compositions, the Pb atoms were displaced in the M_B directions. Here at high temperature, the same phenomenon takes place for PZ.

Both high-temperature disordering for Pb and oxygen octahedra are observed in $PbZrO_3$, but we do not observe significant diffuse scattering in the room-temperature neutron scattering patterns. In the room-temperature *Pbam* phase, the Pb atoms are displaced in the orthorhombic directions, and all the oxygen octahedra tilt in antiphase about the *a* and *b* pseudocubic axes. Therefore, both types of disorder tend to disappear, or at least become less pronounced, when the temperature decreases. In this condensation process, the antiferroelectric phase is stabilized and the ferroelectric phase is disfavoured. On the other hand, in Zr-rich PZT, the two types of disorder are maintained in the lower-temperature *R*3*m* and *R*3*c* phases according to our PDF and DS experiments. This is consistent with the fact that addition of Ti not only greatly increases the range of the ferroelectric phase but also stimulates an increase in the degree of short-range order/disorder in the system.

Acknowledgements

This work was supported by the United States Office of Naval Research (ONR, grant No. N00014-12-1-1045), the Natural Science and Engineering Research Council of Canada (NSERC), and the Czech Science Foundation (project No. 13-15110S). The computational part of this research was undertaken on the NCI National Facility in Canberra, Australia, which is supported by the Australian Commonwealth Government. We are grateful to the Science and Technology Facilities Council (STFC), UK, for access to the ISIS facilities.

References

Boysen, H. (1992). *NIST Spec. Publ.* **846**, 165–174.
Burkovsky, R. G., Bronwald, Y. A., Filimonov, A. V., Rudskoy, A. I., Chernyshov, D., Bosak, A., Hlinka, J., Long, X., Ye, Z.-G. & Vakhrushev, S. B. (2012). *Phys. Rev. Lett.* **109**, 097603.
Burkovsky, R. G., Tagantsev, A. K. *et al.* (2014). *Phys. Rev. B*, **90**, 144301.
Corker, D. L., Glazer, A. M., Dec, J., Roleder, K. & Whatmore, R. W. (1997). *Acta Cryst.* B**53**, 135–142.
Dai, X., Li, J.-F. & Viehland, D. (1995). *Phys. Rev. B*, **51**, 2651–2655.
Fujishita, H. & Hoshino, S. (1984). *J. Phys. Soc. Jpn*, **53**, 226–234.
Fushimi, S. & Ikeda, T. (1967). *J. Am. Ceram. Soc.* **50**, 129–132.
Glazer, A. M. (1972). *Acta Cryst.* B**28**, 3384–3392.
Glazer, A. M. (1975). *Acta Cryst.* A**31**, 756–762.
Glazer, A. M., Roleder, K. & Dec, J. (1993). *Acta Cryst.* B**49**, 846–852.
Gutmann, M. (2005). *Acta Cryst.* A**61**, C164.
Hlinka, J., Ondrejkovic, P., Kempa, M., Borissenko, E., Krisch, M., Long, X. & Ye, Z.-G. (2011). *Phys. Rev. B*, **83**, 140101.
Hlinka, J., Ostapchuk, T., Buixaderas, E., Kadlec, C., Kuzel, P., Gregora, I., Kroupa, J., Savinov, M., Klic, A., Drahokoupil, J., Etxebarria, I. & Dec, J. (2014). *Phys. Rev. Lett.* **112**, 197601.
Íñiguez, J., Stengel, M., Prosandeev, S. & Bellaiche, L. (2014). *Phys. Rev. B*, **90**, 220103.
Keeble, D. S., Barney, E. R., Keen, D. A., Tucker, M. G., Kreisel, J. & Thomas, P. A. (2013). *Adv. Funct. Mater.* **23**, 185–190.
Keen, D. A., Gutmann, M. J. & Wilson, C. C. (2006). *J. Appl. Cryst.* **39**, 714–722.
Kiat, J.-M., Baldinozzi, G., Dunlop, M., Malibert, C., Dkhil, B., Ménoret, C., Masson, O. & Fernandez-Diaz, M.-T. (2000). *J. Phys. Condens. Matter*, **12**, 8411–8425.
Kittel, C. (1951). *Phys. Rev.* **82**, 729–732.
Ko, J.-H., Górny, M., Majchrowski, A., Roleder, K. & Bussmann-Holder, A. (2013). *Phys. Rev. B*, **87**, 184110.
Kuroiwa, Y., Terado, Y., Kim, S. J., Sawada, A., Yamamura, Y., Aoyagi, S., Nishibori, E., Sakata, M. & Takata, M. (2005). *Jpn. J. Appl. Phys.* **44**, 7151–7155.
Mani, B. K., Lisenkov, S. & Ponomareva, I. (2015). *Phys. Rev. B*, **91**, 134112.
Paściak, M., Welberry, T. R., Heerdegen, A. P., Laguta, V., Ostapchuk, T., Leoni, S. & Hlinka, J. (2015). *Phase Transitions*, **88**, 273–282.
Paściak, M., Welberry, T. R., Kulda, J., Kempa, M. & Hlinka, J. (2012). *Phys. Rev. B*, **85**, 224109.
Petricek, V., Dusek, M. & Palatinus, L. (2014). *Z. Kristallogr.* **229**, 345–352.
Proffen, Th. & Neder, R. B. (1997). *J. Appl. Cryst.* **30**, 171–175.
Reyes-Lillo, S. E. & Rabe, K. M. (2013). *Phys. Rev. B*, **88**, 180102.
Sawaguchi, E. & Kittaka, T. (1952). *J. Phys. Soc. Jpn*, **7**, 336–337.
Scott, B. A. & Burns, G. (1972). *J. Am. Ceram. Soc.* **55**, 331–333.
Sepliarsky, M., Asthagiri, A., Phillpot, S. R., Stachiotti, M. G. & Migoni, R. L. (2005). *Curr. Opin. Solid State Mater. Sci.* **9**, 107–113.
Shirane, G., Sawaguchi, E. & Takagi, Y. (1951). *Phys. Rev.* **84**, 476–481.
Tagantsev, A. K. *et al.* (2013). *Nat. Commun.* **4**, 2229.
Tan, X., Ma, C., Frederick, J., Beckman, S. & Webber, K. G. (2011). *J. Am. Ceram. Soc.* **94**, 4091–4107.
Teslic, S. & Egami, T. (1998). *Acta Cryst.* B**54**, 750–765.
Todorov, I. T., Smith, W., Trachenko, K. & Dove, M. T. (2006). *J. Mater. Chem.* **16**, 1911–1918.
Vanderbilt, D. & Cohen, M. H. (2001). *Phys. Rev. B*, **63**, 094108.
Viehland, D. (1995). *Phys. Rev. B*, **52**, 778–791.
Welberry, T. R., Gutmann, M. J., Woo, H., Goossens, D. J., Xu, G., Stock, C., Chen, W. & Ye, Z.-G. (2005). *J. Appl. Cryst.* **38**, 639–647.
Woodward, D. I., Knudsen, J. & Reaney, I. M. (2005). *Phys. Rev. B*, **72**, 104110.
Xie, Y. (2013). PhD thesis, Simon Fraser University, Burnaby, Canada.
Xu, Z., Dai, X., Li, J.-F. & Viehland, D. (1995). *Appl. Phys. Lett.* **66**, 2963–2965.
Zhang, N., Yokota, H., Glazer, A. M., Ren, Z., Keen, D. A., Keeble, D. S., Thomas, P. A. & Ye, Z.-G. (2014). *Nat. Commun.* **5**, 5231.
Zhang, N., Yokota, H., Glazer, A. M. & Thomas, P. A. (2011). *Acta Cryst.* B**67**, 461–466.